



22 relative humidity of the entrained air. Second, the parameterization is implemented in
23 a microphysics scheme in a large eddy simulation model. Third, sensitivity experiments
24 are conducted to compare the new parameterization with the default homogeneous
25 entrainment-mixing parameterization. The results indicate that the new entrainment-
26 mixing parameterization has a larger impact on the number concentration, volume-
27 mean radius, and cloud optical depth in the stratocumulus case than in the cumulus case.
28 This is because inhomogeneous and homogeneous mixing mechanisms dominate in the
29 stratocumulus and cumulus cases, respectively, which is mainly due to the larger
30 turbulence dissipation rate in the cumulus case. Because stratocumulus clouds break up
31 during the dissipation stage to form cumulus clouds, the effects of this new entrainment-
32 mixing parameterization during the stratocumulus dissipation stage are between those
33 during the stratocumulus mature stage and the cumulus case. A large aerosol
34 concentration can enhance the effects of this new entrainment-mixing parameterization
35 by decreasing the cloud droplet size and evaporation time scale. This study sheds new
36 light on the improvement of entrainment-mixing parameterizations in models.

37

38 **1. Introduction**

39 The process of entrainment and subsequent mixing between clouds and their
40 environment is one of the most uncertain processes in cloud physics, which is thought
41 to be crucial to many outstanding issues, including warm-rain initiation and subsequent
42 precipitation characteristics, cloud-climate feedback, and evaluating the indirect effects



43 of aerosol (Paluch and Baumgardner, 1989; Yum, 1998; Ackerman et al., 2004; Kim et
44 al., 2008; Huang et al., 2008; Del Genio and Wu, 2010; Lu et al., 2011; Lu et al., 2014;
45 Kumar et al., 2013; Zheng and Rosenfeld, 2015; Fan et al., 2016; Gao et al., 2020; Gao
46 et al., 2021; Zhu et al., 2021; Xu et al., 2021; Kumar et al., 2013; Yang et al., 2016;
47 Yang et al., 2021). The most well-studied concepts are homogeneous/inhomogeneous
48 entrainment-mixing mechanisms. During homogeneous mixing, all droplets experience
49 evaporation, and no droplet is evaporated completely. During extremely
50 inhomogeneous mixing, some droplets near the entrained air evaporate completely,
51 while the remaining droplets maintain their original sizes. If the situation is somewhere
52 between these two extreme scenarios, an inhomogeneous mixing process occurs. Some
53 studies suggest that homogeneous mixing is likely to be typical (Jensen et al., 1985;
54 Burnet and Brenguier, 2007; Lehmann et al., 2009), whereas others have claimed that
55 extremely inhomogeneous scenario is dominant (Pawłowska et al., 2000; Burnet and
56 Brenguier, 2007; Haman et al., 2007; Freud et al., 2008; Freud et al., 2011). Different
57 mechanisms can be undistinguishable when the relative humidity in the entrained air is
58 high (Gerber et al., 2008).

59 Some sensitivity studies assuming homogeneous or extremely inhomogeneous
60 mixing have found that different mixing mechanisms can significantly influence the
61 microphysics and radiative properties of clouds (Lasher-Trapp et al., 2005; Grabowski,
62 2006; Chosson et al., 2007; Slawinska et al., 2008). For example, Grabowski (2006)
63 used a cloud-resolving model and found that the amount of solar energy reaching the



64 surface in the pristine case, assuming the homogeneous mixing scenario, is the same as
65 in the polluted case with extremely inhomogeneous mixing. This result was verified by
66 Slawinska et al. (2008) using a large-eddy simulation (LES) model. Although the
67 influence of different mixing mechanisms in simulations is lower when two-moment
68 microphysics schemes are used (Hill et al., 2009; Grabowski and Morrison, 2011;
69 Slawinska et al., 2012; Xu et al., 2020), Hill et al. (2009) also claimed that there are
70 still many uncertainties in the entrainment-mixing process, and the effect of different
71 mixing mechanisms can be more important over the entire cloud life-cycle.

72 In recent years, methods have been developed to describe general entrainment-
73 mixing processes, with homogeneous and extremely inhomogeneous scenarios as
74 special cases (Andrejczuk et al., 2006; Andrejczuk et al., 2009; Lehmann et al., 2009;
75 Lu et al., 2011). Hoffmann et al. (2019) and Hoffmann and Feingold (2019) conducted
76 LES at the subgrid-scale with turbulent mixing, using a linear eddy model. Andrejczuk
77 et al. (2009) used the results of direct numerical simulation (DNS) to establish a
78 relationship between instantaneous microphysical properties and Damköhler number
79 (D_a , Burnet and Brenguier, 2007), and developed a parameterization of the entrainment-
80 mixing process. Lu et al. (2013) developed a parameterization of the entrainment-
81 mixing process based on the relationship between the homogeneous mixing degree (ψ)
82 and transition scale number (N_L) in the explicit mixing parcel model (EMPM), as well
83 as aircraft observation data. Gao et al. (2018) investigated how ψ is related to D_a and
84 N_L in a DNS, to improve the parameterization of the entrainment-mixing process. Luo



85 et al. (2020) simulated more than 12,000 cases with EMPM by changing a variety of
86 parameters affecting entrainment-mixing processes and developed a parameterization
87 that improved the one proposed by Lu et al. (2013).

88 Although several entrainment-mixing parametrizations have been proposed, to the
89 best of our knowledge, only one study (Jarecka et al., 2013) has coupled an entrainment-
90 mixing parameterization with cloud microphysics to consider the change in cloud
91 droplet concentration during the entrainment-mixing process. Jarecka et al. (2013)
92 applied an entrainment-mixing parameterization, in terms of the Damköhler number, to
93 a two-moment microphysics scheme and found small impacts of entrainment-mixing
94 parameterization in shallow cumulus clouds. To further explore the influences of
95 entrainment-mixing processes, this study first modifies the entrainment-mixing
96 parameterization in terms of the transition scale number proposed by Luo et al. (2020)
97 to couple it more easily with microphysics schemes. The parameterization is then
98 implemented in the two-moment Thompson aerosol-aware scheme (Thompson and
99 Eidhammer, 2014). Finally, the effects of parameterization on the physical properties
100 of clouds are examined in both cumulus and stratocumulus clouds.

101 The rest of this paper is organized as follows: Section 2 describes the new
102 entrainment-mixing parameterization, simulated cases, and modelling setup. The major
103 results are presented and discussed in Section 3. The influences of the new entrainment-
104 mixing parameterization on cloud physics and the underlying mechanisms are
105 examined, and the effects of turbulence dissipation rate (ε) and aerosol concentration



106 are also discussed. Some concluding remarks are presented in Section 4.

107

108 **2. Parameterization, simulated cases, and modeling setup**

109 **2.1 The new entrainment-mixing parameterization**

110 According to Morrison and Grabowski (2008), the effect of the entrainment-
111 mixing process on cloud microphysical properties can be expressed as follows:

$$112 \quad N_c = N_{c0} \left(\frac{q_c}{q_{c0}} \right)^\alpha, \quad (1)$$

113 where N_c and N_{c0} are the cloud droplet number concentrations after and before the
114 evaporation process, respectively, and q_c and q_{c0} represent the corresponding cloud
115 water mixing ratios. It is noteworthy that when a new saturation is achieved after
116 evaporation, q_c is determined by q_{c0} , relative humidity, air pressure, and temperature.
117 The parameter α can be pre-set to any value between 0 (homogeneous mixing) and 1
118 (extremely inhomogeneous mixing) to represent a different degree of subgrid-scale
119 mixing homogeneity. In this study, instead of specifying α as a predetermined constant,
120 here it is determined through expressions (Lu et al., 2013; Luo et al., 2020)

$$121 \quad \alpha = 1 - \psi, \quad (2a)$$

$$122 \quad \psi = c \exp(aN_L^b). \quad (2b)$$

123 where a , b and c are the three fitting parameters (Luo et al., 2020). The dimensionless
124 number N_L is a dynamical measure of the degree of subgrid-scale mixing homogeneity
125 (Lu et al., 2011) defined by



126
$$N_L = \frac{L^*}{\eta}, \quad (3a)$$

127
$$\eta = (v^3 / \varepsilon)^{1/4}, \quad (3b)$$

128
$$L^* = \varepsilon^{-1/2} \tau_{\text{evap}}^{3/2}, \quad (3c)$$

129 where L^* is the transition length (Lehmann et al., 2009), η is the Kolmogorov microscale,
130 ν is the kinematic viscosity; ε is estimated following the method of Andrejczuk et al.
131 (2009):

132
$$\varepsilon = \left\langle \frac{1}{3} (u^2 + v^2 + w^2) \right\rangle^{3/2} / L, \quad (4)$$

133 where u , v , and w are the characteristic velocities in the horizontal and vertical
134 directions, respectively, and L is the model grid size. The evaporation time scale (τ_{evap})
135 is defined as the time taken for droplets to evaporate completely in an unsaturated
136 environment, and is calculated as

137
$$\tau_{\text{evap}} = -\frac{r^2}{2AS_e}, \quad (5a)$$

138
$$A = \frac{1}{\left[\left(\frac{L_h}{R_v T} - 1 \right) \frac{L_h \rho_L}{KT} + \frac{\rho_L R_v T}{De_s(T)} \right]}, \quad (5b)$$

139 where r is the volume-mean radius of cloud droplets, A is a function of pressure and
140 temperature, S_e is the sub-saturation (relative humidity RH-1) of entrained air, L_h is the
141 latent heat, R_v is the specific gas constant for water vapour, T is air temperature, ρ_L is
142 the density of liquid water, K is the coefficient of thermal conductivity of air, D is the
143 diffusion coefficient of water vapour in the air, and $e_s(T)$ is the saturation vapour
144 pressure over a plane water surface at temperature T .



145 Unfortunately, S_e in Equation (5a) is generally unavailable in atmospheric models,
146 including LES models. Thus, the entrainment-mixing parameterization developed by
147 Luo et al. (2020) based on the properties of entrained air cannot be used directly. To
148 solve this problem, we modify the entrainment-mixing parameterization of Luo et al.
149 (2020) by replacing S_e with the domain-averaged relative humidity in the EMPM, after
150 entrainment but before evaporation, based on 12,218 cases:

$$151 \quad \psi = 107.19 \exp(-1.99 N_L^{-0.29}). \quad (6)$$

152 Figure 1 shows the fitting results of the modified new entrainment-mixing
153 parameterization. Compared to the parametrization proposed by Luo et al. (2020), the
154 modified parameterization has similar ψ - N_L distributions, but with a larger N_L for the
155 same ψ , because the EMPM domain-averaged RH is larger than the entrained-air RH.
156 With this modification, N_L , ψ , and thus the effect of the entrainment-mixing processes
157 on droplet concentration can be directly calculated using the LES grid RH. It is
158 important to note that we do not assume that the RH of entrained air is equal to that of
159 the LES grid. Such a modification is only for the convenience of parameterization
160 applications in microphysics schemes. The details of the EMPM simulations and related
161 calculations are provided by Luo et al. (2020).

162

163 2.2 LES model, simulation cases, and modelling setup

164 The LES model is built by applying the large-scale forcing module presented in
165 Endo et al., 2015) to the Weather Research and Forecasting (WRF) model tailored for



166 solar irradiance forecasting (WRF-Solar, Hacker et al., 2016; Haupt et al., 2016). The
167 large-scale forcing data (VARANAL) used in this process is derived from the
168 constrained variational analysis (CVA) approach developed by Zhang et al. (2001) and
169 provided by the U.S. Department of Energy's Atmospheric Radiation Measurement
170 Program (www.arm.gov). The modified entrainment-mixing parameterization is
171 implemented in the two-moment Thompson aerosol-aware scheme (Thompson and
172 Eidhammer, 2014).

173 To investigate the behaviours of the new entrainment-mixing parameterization in
174 different cloud types, cumulus and stratocumulus cases are simulated. For both the
175 cumulus and stratocumulus cases, the horizontal resolution of the model is $100\text{ m} \times 100$
176 m with a domain area of $14.4\text{ km} \times 14.4\text{ km}$. The vertical direction is divided into 225
177 layers with a resolution of 30 m.

178 For each cloud case, ψ is first set to 1 for the *default* experiment because most LES
179 models assume a homogeneous entrainment-mixing mechanism. The simulation with
180 the new entrainment-mixing parameterization (Equations (1-6)) is hereafter referred to
181 as *new*. First, N_L is diagnosed for each grid, and ψ is then calculated using Equation (6).
182 Finally, the variation in N_c during entrainment-mixing is obtained using Equations (1)
183 and (2a).

184 Considering the significant impacts of ε and initial droplet number concentration
185 on the entrainment-mixing process (Luo et al., 2020; Lu et al., 2013; Grabowski, 2006;
186 Hoffmann and Feingold, 2019), an alternative method that calculates ε from the subgrid



187 turbulent kinetic energy (Deardorff, 1980) is also investigated and is referred to as
188 *new_tke*:

$$189 \quad \varepsilon = CE^{3/2} / L, \quad (7)$$

190 where $C = 0.70$ is an empirical constant and E is the subgrid turbulent kinetic energy.
191 To examine the influence of the aerosol number concentration on the entrainment-
192 mixing process, we conduct the numerical experiments *default_10* and *new_10* by
193 multiplying the initial aerosol number concentrations, for the *default* and *new* models,
194 respectively, by a factor of 10. Thus, five sets of numerical experiments are conducted
195 for both the cumulus and stratocumulus cases; the names of the experiments and
196 corresponding descriptions are summarized in Table 1.

197

198 **3. Results**

199 **3.1 Cumulus case**

200 For the cumulus case, the simulation starts at 9:00 UTC on 11 June 2016 and ends
201 at 03:00 UTC on 12 June 2016 with an output interval of 10 min and spin-times of 3 h.
202 Figure 2 shows the temporal evolution of the cloud fraction from the five numerical
203 experiments. Grid points with q_c larger than 0.01 g/kg are defined as “cloudy areas”.
204 Also shown for comparison is observational data with a one-hour temporal resolution,
205 which is provided by the LES Atmospheric Radiation Measurement Symbiotic
206 Simulation and Observation (LASSO) campaign (Gustafson et al., 2020). The
207 observations show that the cloud forms at 12:00 UTC on 11 June and dissipates



208 completely by 01:00 UTC on 12 June with a maximum cloud fraction of 0.47 at 16:00
209 UTC on 11 June. All simulations capture the evolution of the cloud fraction and exhibit
210 similar values to the observational data.

211 Figure 3 shows the evolution of the microphysical and optical properties of clouds
212 in the cloudy areas of all simulation experiments, including q_c , N_c , droplet volume-
213 mean radius (r_v), cloud water path (CWP), and cloud optical depth (τ). To visually and
214 simultaneously compare the change in cloud droplet concentration under different
215 aerosol concentrations, the maximum cloud droplet concentration (N_{cmax}) from *default*
216 is used to normalize N_c in *default*, *new*, and *new_tke*, while N_{cmax} from *new_10* is used
217 to normalize N_c in *default_10* and *new_10*. The CWP is calculated as:

$$218 \quad CWP = \int_0^H \rho_a q_c(z) dz, \quad (8)$$

219 where ρ_a is the air density, $q_c(z)$ is the cloud water mixing ratio at each height (z), and
220 H is the cloud thickness. The optical depth τ is estimated with

$$221 \quad \tau = \frac{3}{2} \frac{1}{\rho_w} \int_0^H \frac{\rho_a q_c(z)}{r_c(z)} dz, \quad (9)$$

222 where ρ_w is the water density and $r_c(z)$ is the effective radius of the cloud droplets at
223 each height (z). The time-averaged values of these physical properties of the clouds are
224 listed in Table 2 for convenience.

225 For the low aerosol number concentration, the simulations with the new
226 entrainment-mixing parameterization have smaller N_c (34.91 cm^{-3} and 35.53 cm^{-3} for
227 *new* and *new_tke*, respectively) and larger r_v ($13.34 \text{ }\mu\text{m}$ and $13.29 \text{ }\mu\text{m}$ for *new* and
228 *new_tke*, respectively) than the default homogeneous simulation (35.78 cm^{-3} for N_c and



229 13.27 μm for r_v in *default*). However, comparing *new* to *default*, the relative changes in
230 N_c (−2.43%), r_v (+0.53%), and τ (−0.99%) are small. The relative changes in *new_the*
231 are even smaller. When the aerosol concentration increases ten-fold (*default_10* and
232 *new_10*), q_c , CWP, and τ increase according to the aerosol indirect effect (Peng et al.,
233 2002; Wang et al., 2019; Li et al., 2011; Wang et al., 2011). Meanwhile, r_v decreases
234 significantly owing to the larger cloud number concentration. The effects of the new
235 entrainment-mixing parameterization also increase, for example, the change in N_c
236 increases from −2.43% (*new* compared to *default*) to −4.45% (*new_10* compared to
237 *default_10*), r_v increases from +0.53% to +0.85%, and τ from −0.99% to −1.18%; the
238 reasons for these changes are discussed later. These small changes are similar to those
239 identified in previous cumulus studies (Jarecka et al., 2013; Hoffmann et al., 2019).

240

241 3.2 Stratocumulus case

242 The stratocumulus case is simulated from 9:00 UTC on 19 April 2009 to 03:00
243 UTC on 20 April 2009; the first three hours are set to be spin-up times. We examine the
244 stratocumulus region of the cloud base at ~ 2.1 km and the cloud top at ~ 2.3 km (cloud
245 thickness of ~ 200 m). The time series of the cloud fraction in the observed values and
246 five simulated datasets from 12:00 UTC to 24:00 UTC are shown in Figure 4. The
247 observed data show that the cloud fraction increases with time and peaks at 16:00 UTC.
248 All the simulations capture the main features of the cloud fraction. The simulated cloud
249 fraction has a value of 1 before 16:00 UTC, fluctuates from 16:00 UTC to 21:00 UTC,



250 and decreases sharply after 21:00 UTC. This period can be divided into three stages,
251 namely the mature stage, pre-dissipation stage, and dissipation stage.

252 As with the cumulus case, the temporal evolutions of the physical properties (q_c ,
253 N_c , r_v , CWP, and τ) of the clouds are shown in Figure 5. In contrast to the oscillating
254 changes exhibited by the physical quantities in the cumulus case (Figure 3), the physical
255 properties in the stratocumulus case exhibit a mostly smooth temporal evolution.
256 Furthermore, *default* and *new* exhibit clear distinctions during the early periods, but
257 these differences decrease during the dissipation stage. This is also the case with
258 *default_10* and *new_10*.

259 To compare the different behaviours of the simulation experiments at different
260 stages, the results at the mature and dissipation stages are analysed in detail. The mean
261 values of the main microphysical and optical properties of the clouds are summarised
262 in Table 3. As expected, the cloud microphysical and optical properties at the mature
263 stage are all larger than those at the dissipation stage. The effects of the new
264 entrainment-mixing parametrization are also more significant at the mature stage.
265 Compared to *default*, the *new* model results in a 7.27% smaller N_c , 2.42% larger r_v , and
266 5.77% smaller τ during the mature stage. During the dissipation stage, the changes in
267 N_c , r_v , and τ are -4.35%, +0.80%, and -2.56%, respectively. In contrast to the cumulus
268 case, *new_10* is close to *new* and even has a slightly larger influence on cloud properties
269 than *new*, when compared to *default*, during both stages. The largest influence of the
270 new entrainment-mixing parametrization occurs during the mature stage when the



271 aerosol concentration is ten times greater. The differences in N_c , r_v , and τ between
272 *new_10* and *default_10* are -9.67% , $+2.91\%$, and -5.39% , respectively, averaged over
273 the mature stage. The maximum differences in N_c , r_v , and τ are -10.71% , $+6.37\%$, and
274 -7.72% , respectively. These differences are much larger than those reported by Hill et
275 al. (2009) who found that assuming extremely inhomogeneous mixing has a negligible
276 effect on stratocumulus simulations. Our results also prove the speculation of Hill et al.
277 (2009) that the mixing process might play an important role when the stratocumulus is
278 thin (~ 200 m in this study). Furthermore, implementing the new entrainment-mixing
279 parameterization has similar effects on cloud properties to those described by Hoffmann
280 and Feingold (2019) who used the linear eddy model to represent subgrid-scale
281 turbulent mixing. Note that stratocumulus clouds occur in most regions around the
282 world and are important contributors to the surface radiation budget (Wood, 2012;
283 Zheng et al., 2016; Wang et al., 2021; Wang and Feingold, 2009). Stratocumulus clouds
284 dominate in some regions and occur over 60% of the time as vast long-lived sheets,
285 such as the *semi-permanent subtropical marine stratocumulus sheets* (Wood, 2012). In
286 these regions, a 5.39% – 5.77% decrease in τ , caused by the new entrainment-mixing
287 parameterization is expected to have significant effects on the simulation of regional
288 radiative properties and climate change.

289 The averaged influences of the new entrainment-mixing parametrization over all
290 the simulation periods are also examined (Table 4). Quantitatively, the effect of the new
291 entrainment-mixing parameterization is much greater on stratocumulus clouds than on



292 cumulus clouds. Compared to *default*, *new* has an average change of -5.90% in N_c ,
293 $+1.49\%$ in r_v , and -3.98% in τ . When the aerosol concentration increases ten-fold, the
294 differences in N_c , r_v , and τ between *default_10* and *new_10* are -8.97% , $+2.77\%$, and
295 -3.56% , respectively. These differences are larger than the largest changes in the
296 cumulus case.

297

298 **3.3 Mechanisms of the effects of the new entrainment-mixing parameterization**

299 The different effects of the new entrainment-mixing parameterization on different
300 types of clouds and even on different stages of stratocumulus clouds are likely be related
301 to variations in the dominant mixing mechanism. To confirm this, we calculate the
302 average ψ at all grid points experiencing evaporation, the proportion of inhomogeneous
303 mixing grid points to all grid points experiencing evaporation, and the average ψ at the
304 inhomogeneous mixing grid points in *new*, *new_tke*, and *new_10* (Table 5) for the
305 cumulus case, and mature and dissipation stages in the stratocumulus case.

306 For the cumulus case, all three simulations exhibit large ψ and a small proportion
307 of inhomogeneous mixing, indicating that homogeneous mixing is the dominant
308 entrainment-mixing mechanism in all three simulations (Luo et al., 2020; Lu et al.,
309 2013), especially in *new_tke*. Correspondingly, the influences of the new entrainment-
310 mixing parameterization on the cloud physical properties are not significant, as shown
311 in Figure 3 and Table 2. The *new_10* model exhibit a smaller average ψ and a larger
312 proportion of inhomogeneous mixing than *new* and *new_tke*, which results in larger



313 changes in cloud physics, as mentioned in Section 3.1.

314 For the stratocumulus case, Table 5 shows the average ψ at all grid points
315 experiencing evaporation, the proportion of inhomogeneous mixing grid points to all
316 grid points experiencing evaporation, and the average ψ at the inhomogeneous mixing
317 grid points during the two stages. The mature stage always has a smaller ψ but a larger
318 proportion of inhomogeneous mixing than the dissipation stage. The inhomogeneous
319 mixing process dominates the mature stage in *new* and *new_tke*, because more than 60%
320 of the grid points experience inhomogeneous mixing. The inhomogeneous mixing
321 process is more dominant in *new_10*, because less than 3% of the cloudy grid points
322 experience a homogeneous mixing process during the mature stage, which explains
323 why *new_10* has the largest influence when implementing the new entrainment-mixing
324 parametrization. Meanwhile, the average ψ in both stages is smaller than that in the
325 cumulus case for the same simulation configuration. Thus, the effects of the new
326 entrainment-mixing parameterization are more significant for stratocumulus than for
327 cumulus clouds, especially at the mature stage. It is noted that the average ψ and the
328 proportion of inhomogeneous mixing at the dissipation stage of *new* and *new_tke* in the
329 stratocumulus case are very close to the results of *new_10* in the cumulus case. This is
330 because the cloud fraction decreases sharply during the dissipation stage; the
331 stratocumulus clouds break up and produces cumulus clouds with small cloud droplet
332 radius.

333



334 **3.4 The effects of dissipation rate and aerosol concentration on the entrainment-**
335 **mixing process**

336 Previous studies have shown the notable effects of the dissipation rate and aerosol
337 concentration on the entrainment-mixing process. For example, Luo et al. (2020)
338 changed ε from $10^{-5} \text{ m}^2 \text{ s}^{-3}$ to $10^{-2} \text{ m}^2 \text{ s}^{-3}$ and noted huge differences in the corresponding
339 ψ . Small et al. (2013) compared aircraft observations with different background
340 concentrations and found that higher pollution flights tended to slightly more
341 inhomogeneous mixing; Jarecka et al. (2013) also showed various homogeneities of
342 subgrid mixing when aerosol concentration increases ten-fold. To explain the different
343 behaviours of different simulations with the new entrainment-mixing parameterization,
344 the influences of ε and aerosol concentration are examined. Figure 6 shows the
345 probability distribution functions (PDFs) of ε , r_v , τ_{evap} , and N_L for cloud grids
346 experiencing entrainment-mixing processes in *new*, *new_tke*, and *new_10* for the
347 cumulus and stratocumulus cases, respectively. The PDFs from the mature and
348 dissipation stages of the stratocumulus case are shown in Figure 7.

349

350 **3.4.1 Dissipation rate**

351 According to Equation (3), N_L is a function of $\varepsilon^{3/4}$; hence, the PDF of ε directly
352 affects N_L and further results in different ψ . For the cumulus case, the mean ε (0.0032
353 $\text{m}^2 \text{ s}^{-3}$) in *new* is close to the value of 0.0043 $\text{m}^2 \text{ s}^{-3}$ in *new_tke*; these values are similar
354 to those obtained for cumulus clouds in previous studies (e.g. Lu et al., 2016; Hoffmann



355 et al., 2019). The different ε distributions cause a significant difference in the proportion
356 of inhomogeneous mixing (Table 5). As shown in Figure 1, cloud grids experience a
357 homogeneous mixing process if N_L is larger than $\sim 10^5$, the limited distribution of N_L
358 values less than 10^5 in *new_tke* results in a very small number of cloud grid points
359 undergoing inhomogeneous mixing process. Even at the cloud grid points that undergo
360 inhomogeneous mixing, the average ψ is large (98.62%), because most of the N_L values
361 are larger than 10^3 . Therefore, the cloud properties in *new_tke* are close to those in
362 *default*. The *new* model contains more frequent occurrences of small ε and N_L values,
363 resulting in more cloud grid points undergoing a more inhomogeneous mixing process
364 and exhibiting a smaller ψ , compared to those in the *new_tke* model (Table 5); however,
365 the results of *new* are still close to those of *default*, because of the dominance of N_L
366 values larger than 10^5 .

367 For the stratocumulus case, the mean values of ε ($2.7 \times 10^{-4} \text{ m}^2 \text{ s}^{-3}$ in *new* and
368 $2.9 \times 10^{-4} \text{ m}^2 \text{ s}^{-3}$ in *new_tke*) are an order of magnitude less than those in the cumulus
369 case. Therefore, compared with the cumulus case, the distribution of N_L is reduced in
370 the stratocumulus case, while the peak values of *new* and *new_tke* are similar and almost
371 reach the criterion of inhomogeneous mixing ($\sim 10^5$). For the two stages of
372 stratocumulus clouds, ε is an order of magnitude smaller, but r_v was larger (Figure 7)
373 during the mature stage than during the dissipation stage. According to Equation (5a),
374 droplets with smaller r_v are more prone to complete evaporation and have a smaller τ_{evap} .
375 The combination of smaller ε and larger r_v results in a smaller N_L (Equation (3)). This



376 is the reason for the new entrainment-mixing parametrization having more significant
377 effects during the mature stage than during the dissipation stage. In addition, the
378 similarity of the ε and r_v values during the dissipation stage of the stratocumulus case
379 in *new*, compared to the cumulus case in *new_10* (Figures 6a and 6b), explains the
380 similar average ψ values of these scenarios and the proportion of inhomogeneous
381 mixing (Table 5).

382 Therefore, the distribution of ε has a vital impact on the influence of the new
383 entrainment-mixing parameterization. Smaller values of ε result in the new
384 entrainment-mixing parameterization having a more significant influence. Moreover,
385 the r_v in the stratocumulus case is smaller than that in the cumulus case, which is also
386 conducive to a more inhomogeneous mixing process. These are the reasons why the
387 implementation of the new entrainment-mixing parameterization has a larger influence
388 in the stratocumulus case than in the cumulus case, when compared to a homogeneous
389 mixing mechanism.

390

391 **3.4.2 Aerosol concentration**

392 The aerosol concentration affects the entrainment-mixing process by decreasing
393 the cloud droplet radius. As r_v decreases, the distributions of τ_{evap} in *new_10* moves to
394 a smaller overall value, while the mean value is an order of magnitude smaller than that
395 in *new*, which causes a much smaller N_L because N_L is proportional to $\tau_{\text{evap}}^{3/2}$ (Equations
396 (3a) and (3b)). The larger percentage of smaller N_L values indicates that in *new_10*,



397 more grid points undergo an inhomogeneous mixing process, and the proportion of such
398 grid points is much larger than in the *new* model (Table 5). Therefore, compared to *new*,
399 *new_10* exhibit a smaller ψ and the effects of the new entrainment-mixing
400 parameterization on cloud properties are more obvious, for both the cumulus and
401 stratocumulus cases.

402

403 **4. Concluding remarks**

404 The entrainment-mixing process near cloud edges has important effects on cloud
405 microphysics, but the most commonly used microphysics schemes simply assume one
406 extreme mechanism, that is, homogeneous entrainment-mixing. This study first
407 improves the entrainment-mixing parameterization proposed by Luo et al. (2020),
408 which connects the homogeneous mixing degree and transition scale number to
409 estimate the homogeneity of the subgrid mixing process and its impact on the droplet
410 number concentration. The improved parameterization uses grid-mean relative
411 humidity and can be implemented directly into microphysics schemes; there is no need
412 to know the relative humidity of the entrained air. Second, the modified entrainment-
413 mixing parameterization is implemented in the two-moment Thompson aerosol-aware
414 scheme of the LES version of WRF-Solar, to examine its effects on the microphysical
415 and optical properties of cumulus and stratocumulus clouds. Third, several sensitivity
416 experiments are conducted to investigate the effects of the new entrainment-mixing
417 parameterization under different conditions of turbulence dissipation rate and aerosol



418 number concentration.

419 Unlike the commonly assumed homogeneous mixing scenario, the new
420 entrainment-mixing parameterization produces a smaller cloud droplet number
421 concentration and larger cloud droplet radius, with the degree of difference depending
422 on cloud types and stages. Sensitivity tests show that in the cumulus case, the largest
423 average influence of the new entrainment-mixing parameterization occurs under a high
424 aerosol background, but results in only a 4.45% decrease in cloud droplet number
425 concentration and a 0.85% increase in cloud droplet volume-mean radius. The changes
426 become even smaller with a low aerosol background because of the larger cloud droplet
427 radius. In contrast, the new entrainment-mixing parameterization has a larger influence
428 on the microphysical and optical properties of stratocumulus clouds, especially under a
429 high aerosol background and during the mature stage, with a cloud fraction equal to 1.
430 The largest changes resulting from the new entrainment-mixing parameterization are
431 -9.67% , $+2.91\%$, and -5.39% , for cloud number concentration, cloud droplet volume-
432 mean radius, and cloud optical depth, respectively. The new entrainment-mixing
433 parameterization has less of an influence on the dissipation stage than on the mature
434 stage of the stratocumulus case, but affects this case more than the cumulus case.

435 The varying effects of the new entrainment-mixing parameterization are caused
436 by variations in the dominant entrainment-mixing mechanism between different cloud
437 types and stages. Compared to the cumulus case, the stratocumulus case has a much
438 smaller homogeneous mixing degree and a larger proportion of inhomogeneous mixing



439 grid points, especially during the mature stage, which indicates that the inhomogeneous
440 mixing mechanism dominates in the stratocumulus case, while the homogeneous
441 mixing mechanism dominates in the cumulus case. As mentioned above, the changes
442 in physical properties of stratocumulus clouds in the dissipation stage are between those
443 in the mature stage and those of the cumulus case; this is because stratocumulus clouds
444 dissipate sharply to form small cumulus clouds, and the degree of homogeneous mixing
445 during the dissipation stage is therefore between that which occurs during the mature
446 stage and the cumulus case.

447 Sensitivity studies show that how turbulence dissipation rate and aerosol
448 concentration are treated in a simulation can have notable effects on the subgrid
449 homogeneity of the mixing process. A larger dissipation rate can accelerate the mixing
450 process, which results in a larger transition scale number and homogeneous mixing
451 degree; and therefore a mostly homogenous mixing mechanism. This is why the
452 cumulus case exhibit smaller changes than the stratocumulus case after the new
453 entrainment-mixing parameterization is implemented. Larger aerosol number
454 concentrations cause a smaller cloud droplet radius. Smaller droplets evaporate more
455 easily, which leads to a smaller transition scale number and a smaller homogeneous
456 mixing degree. Thus, the entrainment-mixing mechanism tends to be inhomogeneous.
457 Therefore, a larger aerosol number concentration increases the influence of the new
458 entrainment-mixing parameterization in both the cumulus and stratocumulus cases.

459 Note that the new entrainment-mixing parameterization could be more important



460 in the LES model if the relative humidity near the cloud is more accurately simulated,
461 because numerical diffusion may humidify the entrained air (Hoffmann and Feingold,
462 2019). The artificially increased relative humidity limits the influences of the new
463 entrainment-mixing parameterization, because homogeneous and inhomogeneous
464 entrainment-mixing processes are close to each other under conditions of high relative
465 humidity.

466

467 **Author contributions.** XX, CL and YL designed the experiments. XX carried out the
468 experiments and conducted the data analysis with contributions from all coauthors. XX,
469 CL, XZ, and SE developed the model code. XX prepared the paper with help from CL,
470 YL, YW, SL, and LZ.

471

472 **Competing interests.** The authors declare that they have no conflict of interest.

473

474 **Acknowledgements.** This research is supported by the National Key Research and
475 Development Program of China (2017YFA0604001), the National Natural Science
476 Foundation of China (41822504, 42175099, 42027804, 41975181, 42075073). Liu is
477 supported by the U.S. Department of Energy Office of Science Biological and
478 Environmental Research as part of the Atmospheric Systems Research (ASR) Program.
479 Brookhaven National Laboratory is operated by Battelle for the U.S. Department of
480 Energy under Contract DE-SC00112704. The large-scale forcing data used in this paper



481 can be downloaded from the U.S. Department of Energy's Atmospheric Radiation
482 Measurement Program with <https://adc.arm.gov/discovery/#/results>. The LASSO data
483 can be downloaded from <https://archive.arm.gov/lassobrowser>.

484

485 **Reference**

- 486 Ackerman, A. S., Kirkpatrick, M. P., Stevens, D. E., and Toon, O. B.: The impact of
487 humidity above stratiform clouds on indirect aerosol climate forcing, *Nature*, 432,
488 1014-1017, 2004.
- 489 Andrejczuk, M., Grabowski, W. W., Malinowski, S. P., and Smolarkiewicz, P. K.:
490 Numerical simulation of cloud-clear air interfacial mixing: Effects on cloud
491 microphysics, *J. Atmos. Sci.*, 63, 3204-3225, doi:10.1175/JAS3813.1, 2006.
- 492 Andrejczuk, M., Grabowski, W. W., Malinowski, S. P., and Smolarkiewicz, P. K.:
493 Numerical simulation of cloud-clear air interfacial mixing: Homogeneous versus
494 inhomogeneous mixing, *J. Atmos. Sci.*, 66, 2493-2500, doi:10.1175/2009JAS2956.1,
495 2009.
- 496 Burnet, F. and Brenguier, J. L.: Observational study of the entrainment-mixing process
497 in warm convective clouds, *J. Atmos. Sci.*, 64, 1995-2011, doi:10.1175/JAS3928.1,
498 2007.
- 499 Chosson, F., Brenguier, J.-L., and Schüller, L.: Entrainment-mixing and radiative
500 transfer simulation in boundary layer clouds, *J. Atmos. Sci.*, 64, 2670-2682,
501 doi:10.1175/JAS3975.1, 2007.
- 502 Deardorff, J.: Stratocumulus-capped mixed layers derived from a three-dimensional
503 model, *Boundary-Layer Meteorol.*, 18, 495-527, 10.1007/BF00119502, 1980.
- 504 Del Genio, A. D. and Wu, J.: The role of entrainment in the diurnal cycle of continental
505 convection, *J. Climate*, 23, 2722-2738, doi: 10.1175/2009JCLI3340.1, 2010.
- 506 Endo, S., Fridlind, A. M., Lin, W., Vogelmann, A. M., Toto, T., Ackerman, A. S.,
507 McFarquhar, G. M., Jackson, R. C., Jonsson, H. H., and Liu, Y.: RACORO continental
508 boundary layer cloud investigations: 2. Large-eddy simulations of cumulus clouds and
509 evaluation with in situ and ground-based observations, *Journal of Geophysical*
510 *Research: Atmospheres*, 120, 5993-6014, 2015.
- 511 Fan, J., Wang, Y., Rosenfeld, D., and Liu, X.: Review of Aerosol-Cloud Interactions:
512 Mechanisms, Significance, and Challenges, *Journal of the Atmospheric Sciences*, 73,
513 4221-4252, 10.1175/jas-d-16-0037.1, 2016.
- 514 Freud, E., Rosenfeld, D., and Kulkarni, J. R.: Resolving both entrainment-mixing and
515 number of activated CCN in deep convective clouds, *Atmos. Chem. Phys.*, 11, 12887-
516 12900, 2011.
- 517 Freud, E., Rosenfeld, D., Andreae, M. O., Costa, A. A., and Artaxo, P.: Robust relations



- 518 between CCN and the vertical evolution of cloud drop size distribution in deep
519 convective clouds, *Atmos. Chem. Phys.*, 8, 1661-1675, 2008.
- 520 Gao, S., Lu, C., Liu, Y., Mei, F., Wang, J., Zhu, L., and Yan, S.: Contrasting Scale
521 Dependence of Entrainment-Mixing Mechanisms in Stratocumulus Clouds,
522 *Geophysical Research Letters*, 47, 10.1029/2020gl086970, 2020.
- 523 Gao, S., Lu, C., Liu, Y., Yum, S. S., Zhu, J., Zhu, L., Desai, N., Ma, Y., and Wu, S.:
524 Comprehensive quantification of height dependence of entrainment mixing between
525 stratiform cloud top and environment, *Atmospheric Chemistry and Physics*, 21, 11225-
526 11241, 2021.
- 527 Gao, Z., Liu, Y., Li, X., and Lu, C.: Investigation of Turbulent Entrainment-Mixing
528 Processes with a New Particle-Resolved Direct Numerical Simulation Model, *J.*
529 *Geophys. Res.*, 123, 2194-2214, 2018.
- 530 Gerber, H. E., Frick, G. M., Jensen, J. B., and Hudson, J. G.: Entrainment, mixing, and
531 microphysics in trade-wind cumulus, *J. Meteorol. Soc. Japan*, 86A, 87-106, 2008.
- 532 Grabowski, W. W.: Indirect impact of atmospheric aerosols in idealized simulations of
533 convective-radiative quasi equilibrium, *J. Climate*, 19, 4664-4682,
534 doi:10.1175/JCLI3857.1, 2006.
- 535 Grabowski, W. W. and Morrison, H.: Indirect Impact of Atmospheric Aerosols in
536 Idealized Simulations of Convective–Radiative Quasi Equilibrium. Part II: Double-
537 Moment Microphysics, *Journal of Climate*, 24, 1897-1912, 10.1175/2010jcli3647.1,
538 2011.
- 539 Gustafson, W. I., Vogelmann, A. M., Li, Z., Cheng, X., Dumas, K. K., Endo, S., Johnson,
540 K. L., Krishna, B., Fairless, T., and Xiao, H.: The Large-Eddy Simulation (LES)
541 Atmospheric Radiation Measurement (ARM) Symbiotic Simulation and Observation
542 (LASSO) Activity for Continental Shallow Convection, *Bulletin of the American*
543 *Meteorological Society*, 101, E462-E479, 10.1175/bams-d-19-0065.1, 2020.
- 544 Hacker, J. P., Jimenez, P. A., Dudhia, J., Haupt, S. E., Ruiz-Arias, J. A., Gueymard, C.
545 A., Thompson, G., Eidhammer, T., and Deng, A.: WRF-Solar: Description and Clear-
546 Sky Assessment of an Augmented NWP Model for Solar Power Prediction, *Bulletin of*
547 *the American Meteorological Society*, 97, 1249-1264, 10.1175/bams-d-14-00279.1,
548 2016.
- 549 Haman, K. E., Malinowski, S. P., Kurowski, M. J., Gerber, H., and Brenguier, J.-L.:
550 Small scale mixing processes at the top of a marine stratocumulus - a case study, *Q. J.*
551 *Roy. Meteor. Soc.*, 133, 213-226, doi:10.1002/qj.5, 2007.
- 552 Haupt, S. E., Kosovic, B., Jensen, T., Lee, J., Jimenez, P., Lazo, J., Cowie, J.,
553 McCandless, T., Pearson, J., and Weiner, G.: The SunCast solar-power forecasting
554 system: the results of the public-private-academic partnership to advance solar power
555 forecasting, National Center for Atmospheric Research (NCAR), Boulder (CO):
556 Research Applications Laboratory, Weather Systems and Assessment Program (US),
557 2016.
- 558 Hill, A. A., Feingold, G., and Jiang, H.: The influence of entrainment and mixing
559 assumption on aerosol-cloud interactions in marine stratocumulus, *J. Atmos. Sci.*, 66,



- 560 1450-1464, 2009.
- 561 Hoffmann, F. and Feingold, G.: Entrainment and mixing in stratocumulus: Effects of a
562 new explicit subgrid-scale scheme for large-eddy simulations with particle-based
563 microphysics, *J. Atmos. Sci.*, 76, 1955-1973, 10.1175/jas-d-18-0318.1, 2019.
- 564 Hoffmann, F., Yamaguchi, T., and Feingold, G.: Inhomogeneous mixing in Lagrangian
565 cloud models: Effects on the production of precipitation embryos, *Journal of the*
566 *Atmospheric Sciences*, 76, 113-133, 2019.
- 567 Huang, J., Lee, X., and Patton, E. G.: A modelling study of flux imbalance and the
568 influence of entrainment in the convective boundary layer, *Boundary-layer meteorology*,
569 127, 273-292, 2008.
- 570 Jarecka, D., Grabowski, W. W., Morrison, H., and Pawlowska, H.: Homogeneity of the
571 subgrid-scale turbulent mixing in large-eddy simulation of shallow convection, *J.*
572 *Atmos. Sci.*, 70, 2751-2767, 2013.
- 573 Jensen, J. B., Austin, P. H., Baker, M. B., and Blyth, A. M.: Turbulent mixing, spectral
574 evolution and dynamics in a warm cumulus cloud, *J. Atmos. Sci.*, 42, 173-192,
575 doi:10.1175/1520-0469(1985)042<0173:TMSEAD>2.0.CO;2, 1985.
- 576 Kim, B.-G., Miller, M. A., Schwartz, S. E., Liu, Y., and Min, Q.: The role of adiabaticity
577 in the aerosol first indirect effect, *J. Geophys. Res.*, 113, D05210, doi:
578 10.1029/2007jd008961, 2008.
- 579 Kumar, B., Schumacher, J., and Shaw, R.: Cloud microphysical effects of turbulent
580 mixing and entrainment, *Theor. Comp. Fluid Dyn.*, 27, 361-376, 2013.
- 581 Lasher-Trapp, S. G., Cooper, W. A., and Blyth, A. M.: Broadening of droplet size
582 distributions from entrainment and mixing in a cumulus cloud, *Q. J. Roy. Meteor. Soc.*,
583 131, 195-220, doi:10.1256/qj.03.199, 2005.
- 584 Lehmann, K., Siebert, H., and Shaw, R. A.: Homogeneous and inhomogeneous mixing
585 in cumulus clouds: dependence on local turbulence structure, *J. Atmos. Sci.*, 66, 3641-
586 3659, doi:10.1175/2009JAS3012.1, 2009.
- 587 Li, Z., Li, C., Chen, H., Tsay, S. C., Holben, B., Huang, J., Li, B., Maring, H., Qian, Y.,
588 and Shi, G.: East Asian studies of tropospheric aerosols and their impact on regional
589 climate (EAST-AIRC): An overview, *Journal of Geophysical Research: Atmospheres*,
590 116, 2011.
- 591 Lu, C., Liu, Y., and Niu, S.: Examination of turbulent entrainment-mixing mechanisms
592 using a combined approach, *J. Geophys. Res.*, 116, D20207,
593 doi:10.1029/2011JD015944, 2011.
- 594 Lu, C., Liu, Y., Niu, S., and Endo, S.: Scale dependence of entrainment-mixing
595 mechanisms in cumulus clouds, *Journal of Geophysical Research: Atmospheres*, 119,
596 13,877-813,890, 2014.
- 597 Lu, C., Liu, Y., Niu, S., Krueger, S., and Wagner, T.: Exploring parameterization for
598 turbulent entrainment-mixing processes in clouds, *Journal of Geophysical Research:*
599 *Atmospheres*, 118, 185-194, 10.1029/2012jd018464, 2013.
- 600 Lu, C., Liu, Y., Zhang, G. J., Wu, X., Endo, S., Cao, L., Li, Y., and Guo, X.: Improving
601 parameterization of entrainment rate for shallow convection with aircraft measurements



- 602 and large eddy simulation, *J. Atmos. Sci.*, 73, 761-773, 10.1175/JAS-D-15-0050.1,
603 2016.
- 604 Luo, S., Lu, C., Liu, Y., Bian, J., Gao, W., Li, J., Xu, X., Gao, S., Yang, S., and Guo, X.:
605 Parameterizations of Entrainment-Mixing Mechanisms and Their Effects on Cloud
606 Droplet Spectral Width Based on Numerical Simulations, *Journal of Geophysical*
607 *Research: Atmospheres*, 125, e2020JD032972, 2020.
- 608 Morrison, H. and Grabowski, W. W.: Modeling supersaturation and subgrid-scale
609 mixing with two-moment bulk warm microphysics, *J. Atmos. Sci.*, 65, 792-812,
610 doi:10.1175/2007JAS2374.1, 2008.
- 611 Paluch, I. R. and Baumgardner, D. G.: Entrainment and fine-scale mixing in a
612 continental convective cloud, *J. Atmos. Sci.*, 46, 261-278, doi:10.1175/1520-
613 0469(1989)046<0261:EAFSMI>2.0.CO;2, 1989.
- 614 Pawlowska, H., Brenguier, J. L., and Burnet, F.: Microphysical properties of
615 stratocumulus clouds, *Atmos. Res.*, 55, 15-33, 2000.
- 616 Peng, Y., Lohmann, U., Leitch, R., Banic, C., and Couture, M.: The cloud albedo-cloud
617 droplet effective radius relationship for clean and polluted clouds from RACE and
618 FIRE.ACE, *J. Geophys. Res.*, 107, AAC 1-1-AAC 1-6, 10.1029/2000JD000281, 2002.
- 619 Slawinska, J., Grabowski, W. W., Pawlowska, H., and Morrison, H.: Droplet activation
620 and mixing in large-eddy simulation of a shallow cumulus field, *J. Atmos. Sci.*, 69, 444-
621 462, 2012.
- 622 Slawinska, J., Grabowski, W. W., Pawlowska, H., and Wyszogrodzki, A. A.: Optical
623 properties of shallow convective clouds diagnosed from a bulk-microphysics large-
624 eddy simulation, *J. Climate*, 21, 1639-1647, 2008.
- 625 Small, J. D., Chuang, P., and Jonsson, H.: Microphysical imprint of entrainment in
626 warm cumulus, *Tellus B*, 65, 6647-6662, 2013.
- 627 Thompson, G. and Eidhammer, T.: A study of aerosol impacts on clouds and
628 precipitation development in a large winter cyclone, *Journal of the atmospheric*
629 *sciences*, 71, 3636-3658, 2014.
- 630 Wang, H. and Feingold, G.: Modeling mesoscale cellular structures and drizzle in
631 marine stratocumulus. Part I: Impact of drizzle on the formation and evolution of open
632 cells, *Journal of the Atmospheric Sciences*, 66, 3237-3256, 2009.
- 633 Wang, M., Ghan, S., Ovchinnikov, M., Liu, X., Easter, R., Kassianov, E., Qian, Y., and
634 Morrison, H.: Aerosol indirect effects in a multi-scale aerosol-climate model PNNL-
635 MMF, *Atmospheric Chemistry and Physics*, 11, 5431-5455, 2011.
- 636 Wang, Y., Zhao, C., McFarquhar, G. M., Wu, W., Reeves, M., and Li, J.: Dispersion of
637 Droplet Size Distributions in Supercooled Non-precipitating Stratocumulus from
638 Aircraft Observations Obtained during the Southern Ocean Cloud Radiation Aerosol
639 Transport Experimental Study, *Journal of Geophysical Research: Atmospheres*, 126,
640 e2020JD033720, 2021.
- 641 Wang, Y., Niu, S., Lv, J., Lu, C., Xu, X., Wang, Y., Ding, J., Zhang, H., Wang, T., and
642 Kang, B.: A new method for distinguishing unactivated particles in cloud condensation
643 nuclei measurements: Implications for aerosol indirect effect evaluation, *Geophysical*



- 644 Research Letters, 46, 14185-14194, 2019.
645 Wood, R.: Review: Stratocumulus Clouds, *Monthly Weather Review*, 140, 2373-2423,
646 2012.
647 Xu, X., Sun, C., Lu, C., Liu, Y., Zhang, G. J., and Chen, Q.: Factors affecting
648 entrainment rate in deep convective clouds and parameterizations, *Journal of*
649 *Geophysical Research: Atmospheres*, 126, e2021JD034881, 2021.
650 Xu, X., Lu, C., Liu, Y., Gao, W., Wang, Y., Cheng, Y., Luo, S., and Van Weverberg, K.:
651 Effects of cloud liquid-phase microphysical processes in mixed-phase cumuli over the
652 Tibetan Plateau, *Journal of Geophysical Research: Atmospheres*, 125, e2020JD033371,
653 2020.
654 Yang, B., Wang, M., Zhang, G. J., Guo, Z., Huang, A., Zhang, Y., and Qian, Y.: Linking
655 Deep and Shallow Convective Mass Fluxes via an Assumed Entrainment Distribution
656 in CAM5-CLUBB: Parameterization and Simulated Precipitation Variability, *Journal*
657 *of Advances in Modeling Earth Systems*, 13, e2020MS002357, 2021.
658 Yang, F., Shaw, R., and Xue, H.: Conditions for super-adiabatic droplet growth after
659 entrainment mixing, *Atmos. Chem. Phys.*, 16, 9421-9433, 10.5194/acp-2016-94, 2016.
660 Yum, S.: Cloud droplet spectral broadening in warm clouds: An observational and
661 model study, Dissertation for the Doctoral Degree, University of Nevada, Reno, Nevada,
662 USA, 191 pp., 1998.
663 Zhang, M. H., Lin, J. L., Cederwall, R. T., Yio, J. J., and Xie, S. C.: Objective analysis
664 of ARM IOP data: Method and sensitivity, *Mon. Weather Rev.*, 129, 295-311,
665 10.1175/1520-0493(2001)129<0295:OAOAID>2.0.CO;2, 2001.
666 Zheng, Y. and Rosenfeld, D.: Linear relation between convective cloud base height and
667 updrafts and application to satellite retrievals, *Geophysical Research Letters*, 42, 6485-
668 6491, 10.1002/2015gl064809, 2015.
669 Zheng, Y., Rosenfeld, D., and Li, Z.: Quantifying cloud base updraft speeds of marine
670 stratocumulus from cloud top radiative cooling, *Geophysical Research Letters*, 43,
671 11,407-411,413, 2016.
672 Zhu, L., Lu, C., Yan, S., Liu, Y., Zhang, G. J., Mei, F., Zhu, B., Fast, J. D., Matthews,
673 A., and Pekour, M. S.: A New Approach for Simultaneous Estimation of Entrainment
674 and Detrainment Rates in Non-Precipitating Shallow Cumulus, *Geophysical Research*
675 *Letters*, 48, 10.1029/2021gl093817, 2021.

676

677



678 Table 1. Summary of names and corresponding descriptions of the five experiments for
 679 each case of cumulus and stratocumulus. The meaning of each symbol for each
 680 experiment can be found in the text.

	Entrainment-mixing parameterization	Dissipation rate	Aerosol number concentration
<i>default</i>	$\alpha = 0$	-	default
<i>new</i>	$\alpha = 1 - \psi,$ $\psi = 107.19 \exp(-1.99 N_L^{-0.29}).$	$\varepsilon = \left\langle \frac{1}{3} (u^2 + v^2 + w^2) \right\rangle^{3/2} / L.$	default
<i>new_tke</i>	$\alpha = 1 - \psi,$ $\psi = 107.19 \exp(-1.99 N_L^{-0.29}).$	$\varepsilon = C E^{3/2} / L.$	default
<i>default_10</i>	$\alpha = 0$	-	default×10
<i>new_10</i>	$\alpha = 1 - \psi,$ $\psi = 107.19 \exp(-1.99 N_L^{-0.29}).$	$\varepsilon = \left\langle \frac{1}{3} (u^2 + v^2 + w^2) \right\rangle^{3/2} / L.$	default×10

681



682 Table 2. Summary of the case mean values of the key quantities in all the simulations
683 of the cumulus case, containing cloud water mixing ratio (q_c), cloud droplet number
684 concentration (N_c), cloud droplet volume-mean radius (r_v), cloud water path (CWP),
685 and cloud optical depth (τ). The experiments are detailed in Table 1.

	<i>default</i>	<i>new</i>	<i>new_tke</i>	<i>default_10</i>	<i>new_10</i>
$q_c(\text{g/kg})$	0.44	0.44	0.44	0.56	0.57
$N_c(\text{cm}^{-3})$	35.78	34.91	35.53	278.80	266.37
$r_v(\mu\text{m})$	13.27	13.34	13.29	7.05	7.11
CWP(g/m^2)	142.30	143.15	144.25	186.52	187.82
τ	13.07	12.94	13.02	31.29	30.92

686

687



688 Table 3. Summary of the case mean values of the key quantities in all the simulations
689 of the stratocumulus case, including cloud water mixing ratio (q_c), cloud droplet number
690 concentration (N_c), cloud droplet volume-mean radius (r_v), cloud water path (CWP),
691 and cloud optical depth (τ). The numbers in and out of the parentheses are the results at
692 the mature and dissipation stages, respectively. The experiments are detailed in Table 1.

	<i>default</i>	<i>new</i>	<i>new_tke</i>	<i>default_10</i>	<i>new_10</i>
$q_c(\text{g/kg})$	0.13	0.13	0.13	0.16	0.16
	(0.039)	(0.039)	(0.039)	(0.041)	(0.041)
$N_c(\text{cm}^{-3})$	35.74	33.14	33.11	256.82	231.98
	(19.76)	(18.90)	(18.82)	(138.74)	(126.99)
$r_v(\mu\text{m})$	10.32	10.57	10.65	5.15	5.30
	(7.53)	(7.59)	(7.69)	(4.02)	(4.11)
CWP(g/m^2)	41.39	41.33	41.78	56.21	57.12
	(2.57)	(2.45)	(2.43)	(2.71)	(2.77)
τ	4.68	4.41	4.40	13.17	12.46
	(0.39)	(0.38)	(0.38)	(0.78)	(0.78)

693



694 Table 4. Cloud water mixing ratio (q_c), cloud droplet number concentration (N_c), cloud
695 droplet volume-mean radius (r_v), cloud water path (CWP), cloud optical depth (τ) in all
696 simulations for the entire lifetime of the stratocumulus case. The experiments are
697 detailed in Table 1.

	<i>default</i>	<i>new</i>	<i>new_tke</i>	<i>default_10</i>	<i>new_10</i>
$q_c(\text{g/kg})$	0.11	0.11	0.11	0.13	0.13
$N_c(\text{cm}^{-3})$	29.98	28.21	28.12	223.65	203.59
$r_v(\mu\text{m})$	9.38	9.52	9.57	5.06	5.20
CWP(g/m^2)	30.78	30.34	29.92	42.22	43.19
τ	4.02	3.86	3.89	10.39	10.02

698

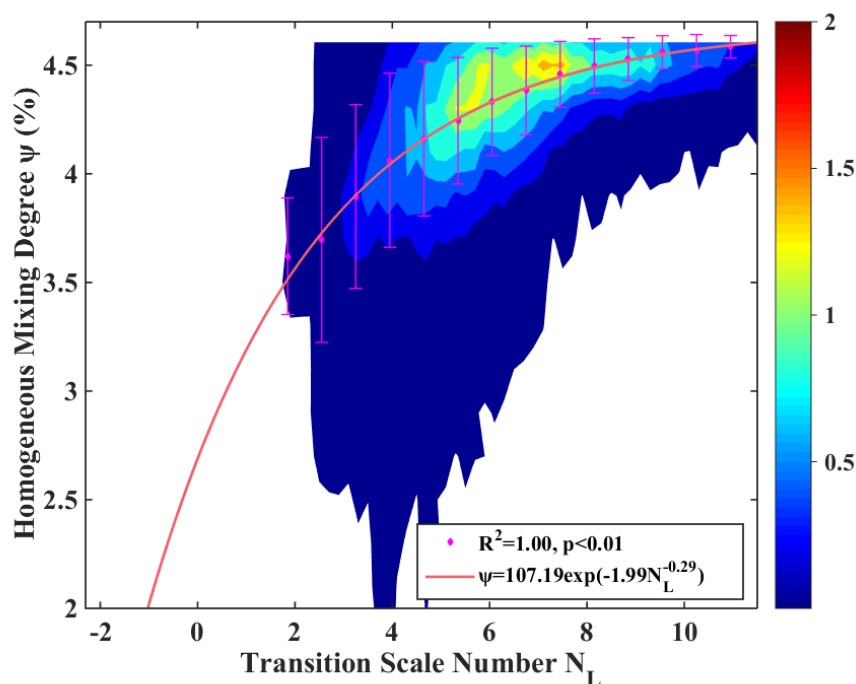
699



700 Table 5. Homogeneous mixing degree (ψ) at all grid points experiencing evaporation,
701 the proportion of inhomogeneous mixing grid points to all grid points experiencing
702 evaporation, and ψ at the inhomogeneous mixing grid points in the experiments *new*,
703 *new_tke* and *new_10* (Table 1) for the cumulus (Cu) and stratocumulus (St) case. The
704 numbers in and out of the parentheses are the results at the mature and dissipation stages
705 in the stratocumulus (St) case, respectively. The experiments are detailed in Table 1.

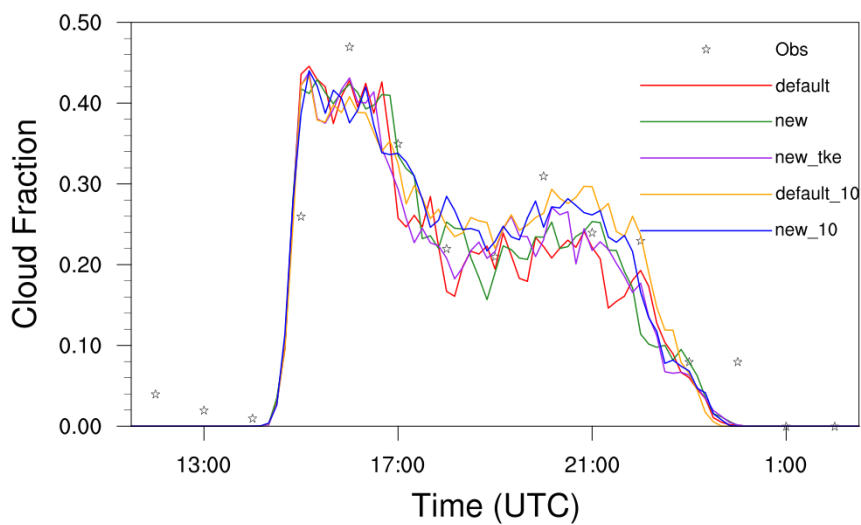
	ψ at all grids (%)	Proportion of inhomogeneous mixing grids (%)	ψ at the inhomogeneous mixing grids (%)
<i>new</i> (Cu)	98.80	13.78	91.21
<i>new_tke</i> (Cu)	99.93	4.52	98.62
<i>new_10</i> (Cu)	94.41	49.32	86.01
<i>new</i> (St)	79.38 (94.12)	60.22 (42.36)	71.33 (90.66)
<i>new_tke</i> (St)	78.56 (94.68)	63.07 (40.61)	71.56 (89.33)
<i>new_10</i> (St)	68.23 (88.22)	97.11 (73.19)	65.18 (85.12)

706



707

708 Figure 1. Parameterization of cloud entrainment-mixing mechanisms by relating
709 homogeneous mixing degree (ψ) to transition scale number (N_L) from EMPM. The
710 contours represent the joint probability distribution function (PDF) of ψ vs N_L . The
711 magenta dots and error bars are mean values and standard deviations of ψ in each N_L
712 bin, respectively. The mean values are fitted using a weighted least squares method with
713 the number of data points in each N_L bin as the weight. The fitting equation, coefficient
714 of determination (R^2), and p -value are also given. N_L is calculated by with the domain-
715 averaged relative humidity after entrainment but before evaporation in the EMPM.



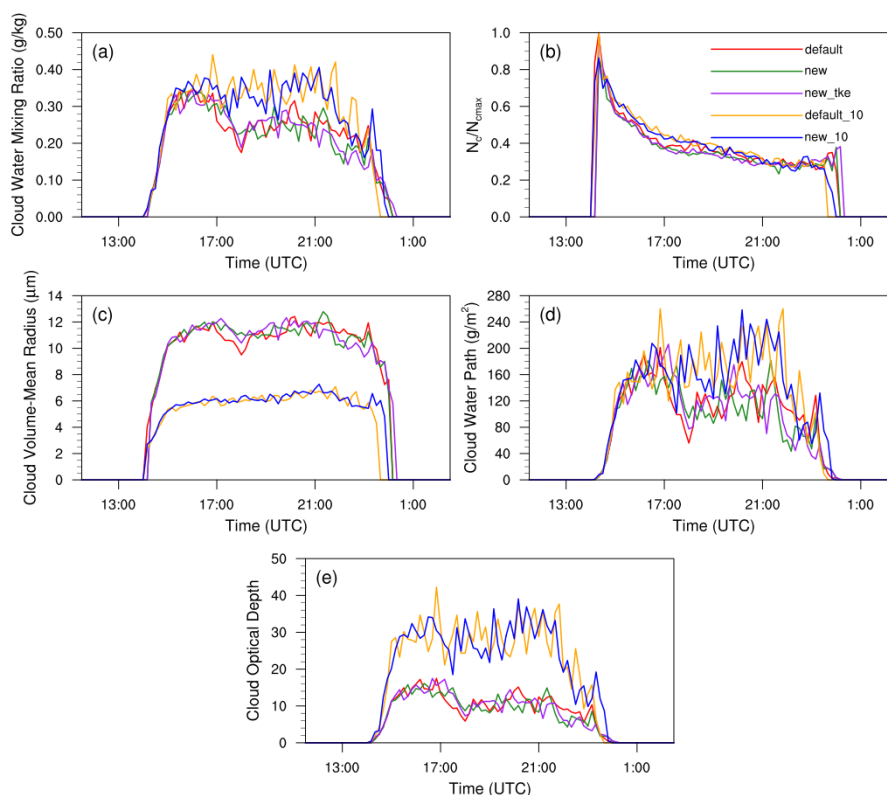
716

717 Figure 2. Time series of cloud fraction from 12:00 UTC on June 11, 2016, to 03:00

718 UTC on June 12, 2016, from the observation in LASSO and five simulation

719 experiments in the cumulus case. The five experiments are detailed in Table 1.

720



721

722 Figure 3. The temporal evolutions of main cloud microphysical and optical properties

723 in all simulation experiments for the cumulus case, including (a) cloud water mixing

724 ratio (q_c) (g/kg), (b) cloud droplet number concentration (N_c) ($/\text{cm}^3$), (c) cloud droplet

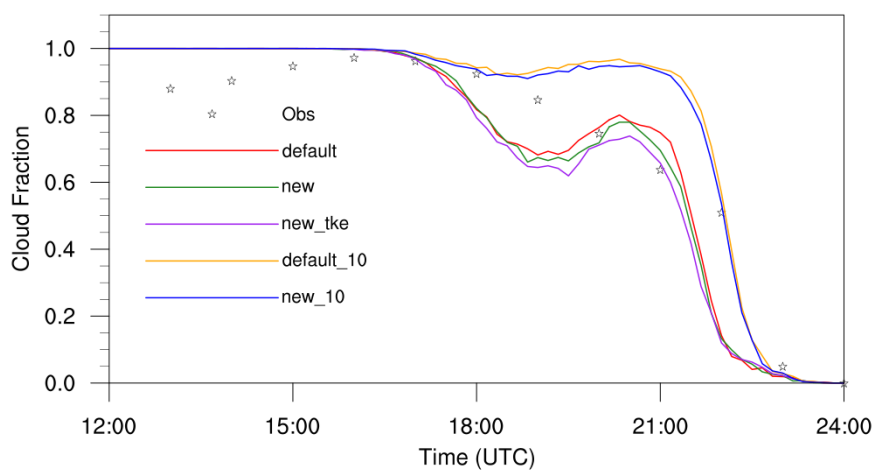
725 volume-mean radius (r_v) (μm), (d) cloud water path (CWP) (g/m^2), and (e) cloud optical

726 depth (τ). In (b), N_c in the experiments *default*, *new*, and *new_tke* are normalized by the

727 maximum cloud droplet concentration (N_{cmax}) from *default*, respectively; N_c in the

728 experiments *default_10* and *new_10* are normalized by N_{cmax} from *default_10*,

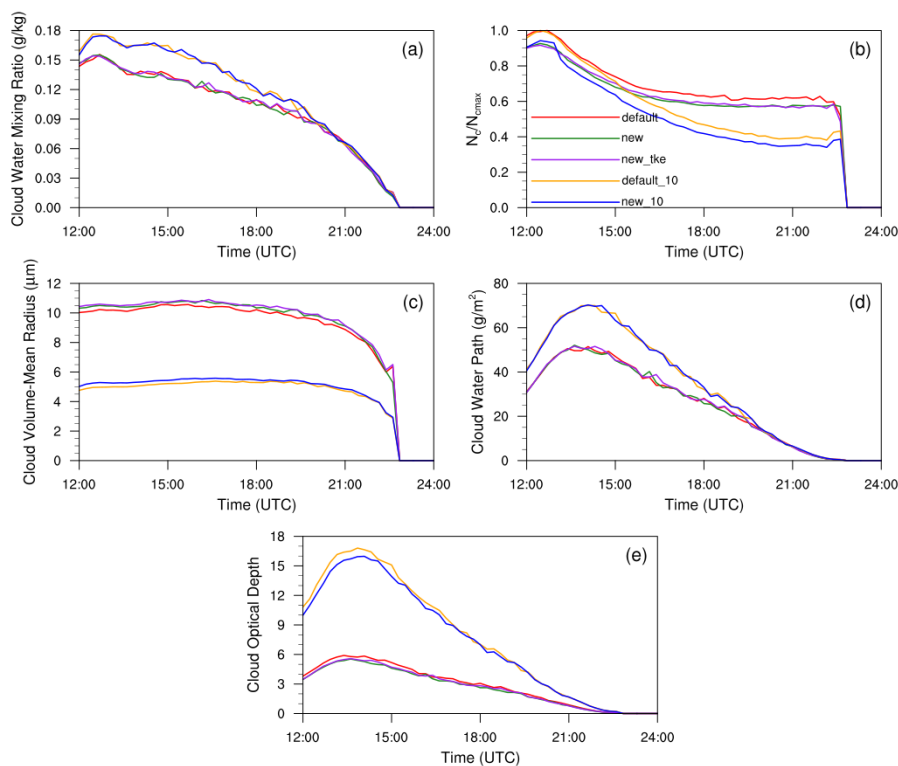
729 respectively. The five experiments are detailed in Table 1.



730

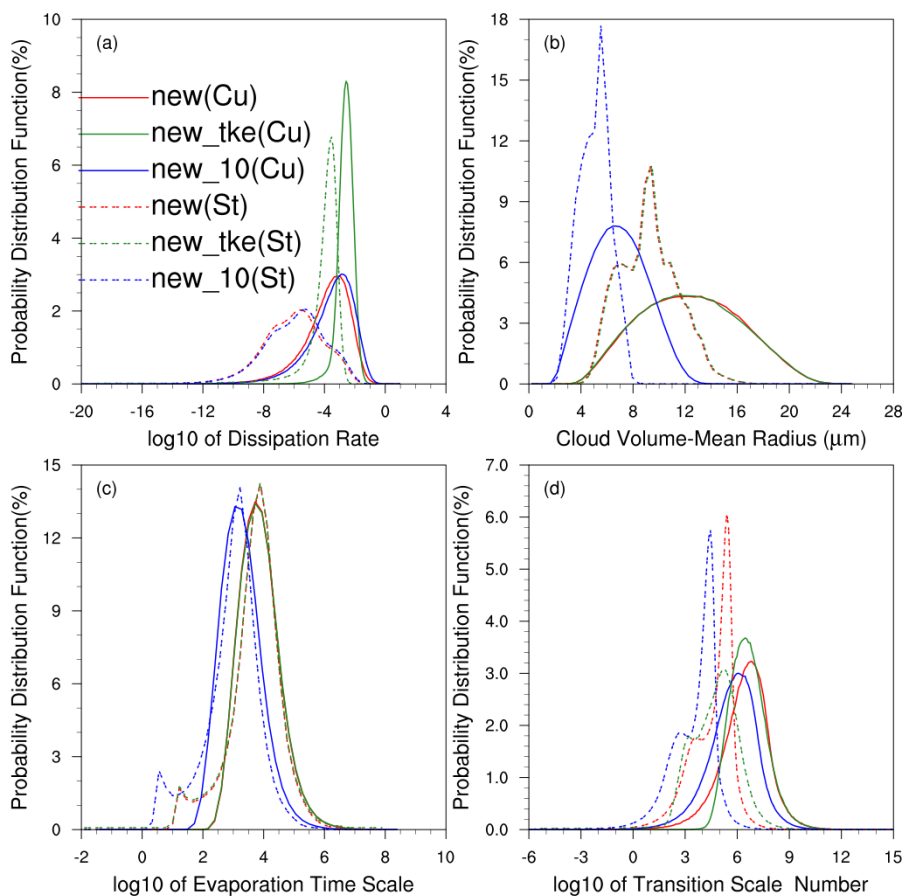
731 Figure 4. Time series of cloud fraction from the observation and five simulations in the

732 stratocumulus case. The five experiments are detailed in Table 1.



733

734 Figure 5. The temporal evolutions of main cloud microphysical and optical properties
735 in all simulation experiments for the stratocumulus case, including (a) cloud water
736 mixing ratio (q_c) (g/kg), (b) cloud droplet number concentration (N_c) ($/\text{cm}^3$), (c) cloud
737 droplet volume-mean radius (r_v) (μm), (d) cloud water path (CWP) (g/m^2), and (e) cloud
738 optical depth (τ). In (b), N_c in the experiments *default*, *new*, and *new_tke* are normalized
739 by the maximum cloud droplet number concentration ($N_{c\text{max}}$) from *default*, respectively;
740 N_c in the experiments *default_10* and *new_10* are normalized by $N_{c\text{max}}$ from *default_10*,
741 respectively. The five experiments are detailed in Table 1.



742

743 Figure 6. Probability distribution functions (PDFs) of (a) turbulence dissipation rate (ϵ),

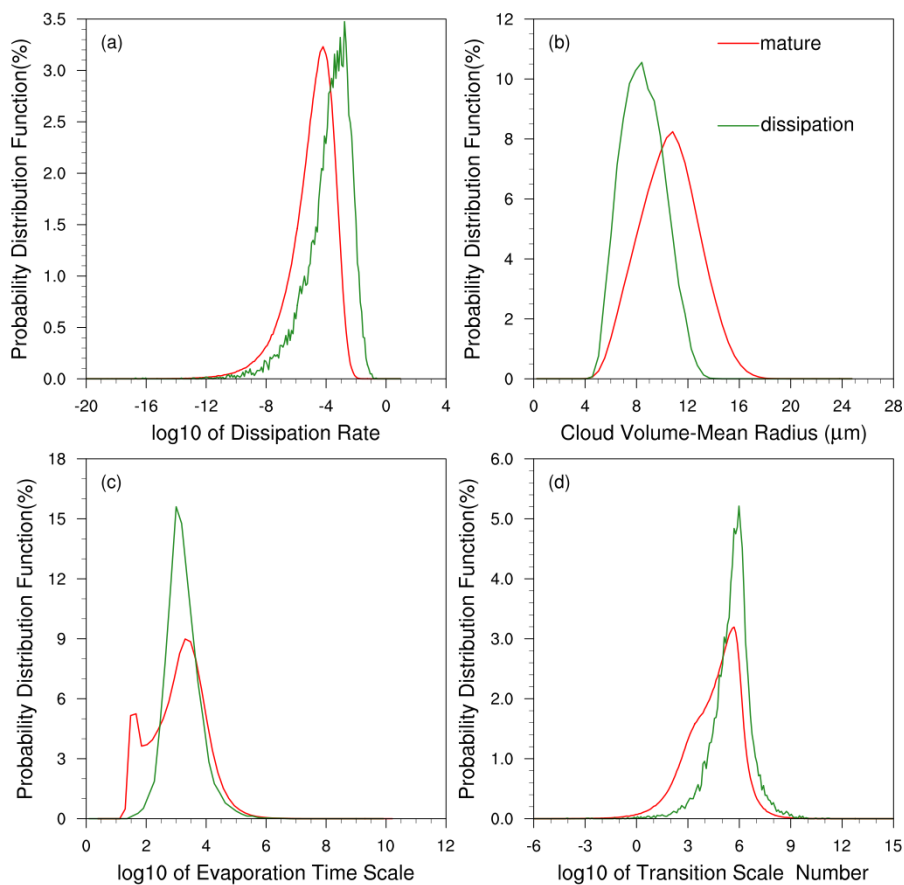
744 (b) cloud droplet volume-mean radius (r_v), (c) evaporation time scale (τ_{evap}), and (d)

745 transition scale number (N_L) of cloud grids experiencing the entrainment-mixing

746 process in the simulations with the new entrainment-mixing parameterization for the

747 cumulus case (Cu, the solid lines) and the stratocumulus case (St, the dash lines),

748 respectively. The experiments are detailed in Table 1.



749

750 Figure 7. Probability distribution functions (PDFs) of (a) turbulence dissipation rate (ϵ),
751 (b) cloud droplet volume-mean radius (r_v), (c) evaporation time scale (τ_{evap}), and (d)
752 transition scale number (N_L) of cloud grids experiencing the entrainment-mixing
753 process at the mature stage from 12:00 UTC to 16:00 UTC (the red lines) and the
754 dissipation stage from 21:00 UTC to 24:00 UTC (the green lines) in *new* for the
755 stratocumulus case. The experiment is detailed in Table 1.